

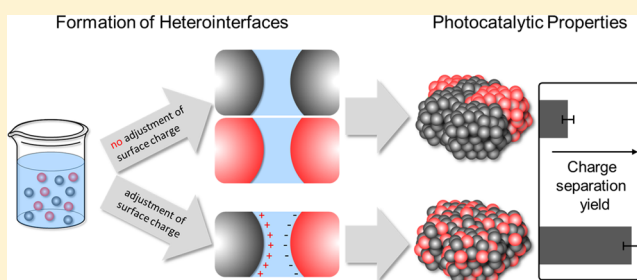
Particle Networks from Powder Mixtures: Generation of TiO_2 – SnO_2 Heterojunctions via Surface Charge-Induced Heteroaggregation

Nicolas Siedl, Stefan O. Baumann, Michael J. Elser, and Oliver Diwald*

Institute of Particle Technology, Friedrich-Alexander University Erlangen-Nuremberg, Cauerstraße 4, 91058 Erlangen, Germany

Supporting Information

ABSTRACT: We explored the impact of interfacial property changes on aggregation behavior and photoinduced charge separation in mixed metal oxide nanoparticle ensembles. TiO_2 and SnO_2 nanoparticles were synthesized by metal organic chemical vapor synthesis and subsequently transformed into aqueous colloidal dispersions using formic acid for adjustment of the particles' surface charge. Surface charge-induced heteroaggregation was found to yield blended nanoparticle systems of exceptionally high mixing quality and, after vacuum annealing, to extremely high concentrations of heterojunctions between TiO_2 and SnO_2 nanoparticles with dehydroxylated surfaces. For tracking charge transfer processes across heterojunctions, the photogeneration of trapped charge carriers was measured with electron paramagnetic resonance (EPR) spectroscopy. On blended nanoparticles systems with high concentrations of SnO_2 – TiO_2 heterojunctions, we observed an enhanced cross section for interparticle charge separation. This results from an effective interfacial charge transfer across the interfaces and gives rise to substantially increased concentrations of electrons and hole centers. The here presented insights are key to the rational design of particle-based heterojunctions and mesoporous nanoparticle networks and help to engineer composite nanomaterials for photocatalysis and solar energy conversion.



INTRODUCTION

An efficient photocatalyst minimizes recombination of photo-excited electron–hole pairs and maximizes electron and hole transfer to the adsorbate upon consecutive surface reactions. In general, the photocatalytic activity of a given particle system depends on multiple factors. For a reliable photoactivity assessment, relative contributions from the particles' bulk and interfaces have to be sorted out, and their impact to the overall performance requires a careful evaluation.^{1–4} A major limitation of any photocatalytic process originates from charge carrier recombination. Efforts have been made to identify and eliminate the responsible defects. An important approach to counteract charge carrier recombination in photocatalytic particle systems is based on the coupling of different semiconductor components with desirable matching of their electronic band structures.^{1,5–11}

In the case of composite nanoparticle systems, synergistic properties and those that are enhanced with respect to the individual components can only emerge if the particles are mixed intimately enough.¹² For that reason, researchers have explored efficient and cost-effective methods for combining different metal oxide nanoparticles. Chemical ways could offer great control in this respect.^{13,14} While a variety of experimental approaches leading to the coupling of two semiconductors have been successfully employed for particles that were grown in colloidal solutions,^{15,16} there are very few reports about the charge separation properties of dry particle systems that feature

corresponding types of interfaces. With this study we present a simple as well as versatile approach that involves surface charging of multiple particle systems inside the same aqueous dispersion medium to achieve blended nanoparticle systems of superior mixing quality and, thus, a maximum concentration of functional interfaces between different particle types.

We have shown in previous work that water-mediated aggregation of TiO_2 and ZrO_2 nanoparticles and subsequent dehydration procedures under high vacuum conditions are effective in the generation of solid–solid interfaces.^{17,18} The mechanistic steps of the underlying material transformation process are as follows (Figure 1): in aqueous dispersion, mutual attraction and agglomeration of metal oxide nanoparticles takes place. Upon vacuum treatment dehydration/dehydroxylation processes (evaporation of liquid phase) in conjunction with particle condensation lead to the formation of chemical interparticle metal oxygen bonds. Annealing-induced aggregation of particles during thermal treatment results in interconnected particles but, according to N_2 sorption measurements, does not reduce the specific surface area in comparison to the unprocessed nanoparticle powders.¹⁷

For the exploration of surface charge-induced heteroaggregation, we chose the TiO_2 – SnO_2 system. Both materials are

Received: August 4, 2012

Revised: September 21, 2012

Published: October 4, 2012



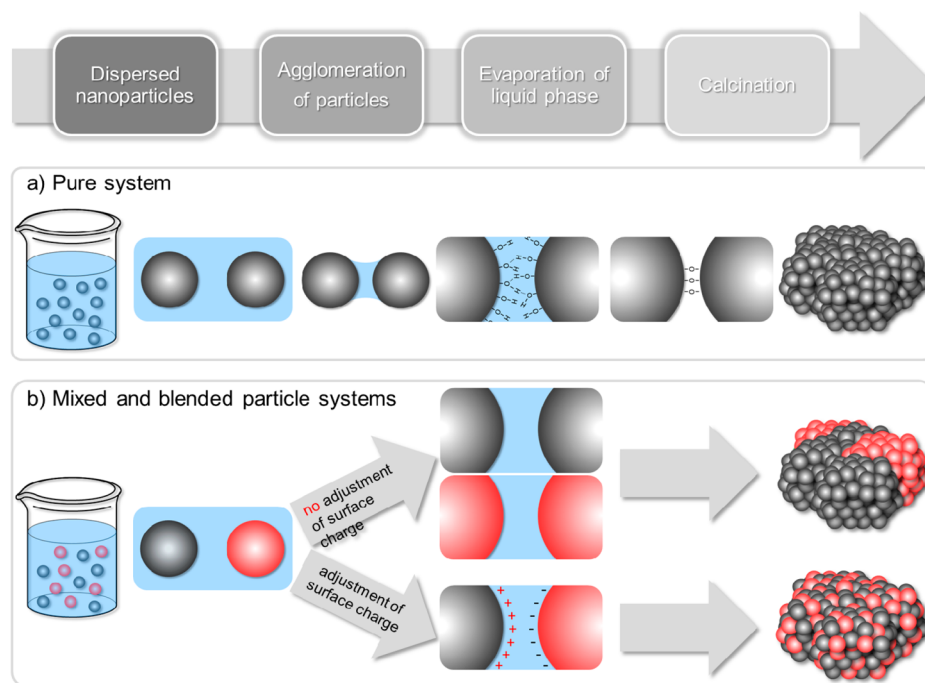


Figure 1. (a) Schematic showing the principle of hydration-dehydration induced particle aggregation and solid–solid interface formation. (b) Adjustment of opposite surface charges on multiple particle types is expected to favor preferential attraction between different particles and yields good mixing qualities.

central to photocatalysis, solar water splitting, and dye sensitized solar cells. As a result of composite formation upon generation of heterointerfaces, light-induced charge separation and vectorial charge transfer (Figure 2) were

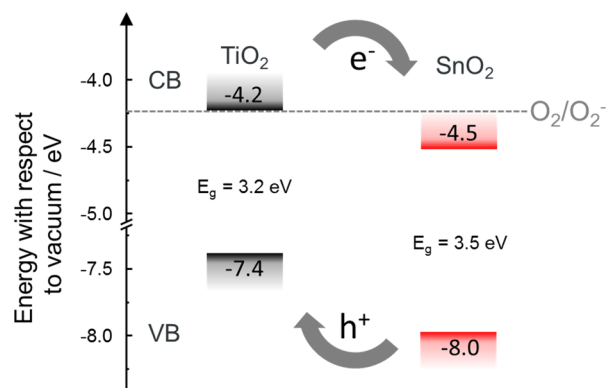


Figure 2. Schematic energy diagram showing the positions of conduction and valence band edges of TiO₂ and SnO₂. Expected vectorial charge transfer directions are indicated for electrons (top arrow) and holes (bottom arrow).

found to be facilitated in composites.¹⁹ The conduction band position of SnO₂ is lower than that of TiO₂ and such that it is incapable of reducing oxygen molecules to form superoxide anions. The band offsets between TiO₂ and SnO₂ will promote charge separation across the interfaces. Using electron paramagnetic resonance (EPR) spectroscopy, we address the vectorial transfer of separated charges to generate paramagnetic O^{•−} radicals as well as paramagnetic Ti³⁺ sites. Another reason for selecting this system has been the exclusion of Sn–Ti–O compound formation. For SnO₂–TiO₂ core–shell nanostructures, it was found that the phase boundary between the two oxides remains abrupt up to $T = 1200$ K without substantial

chemical transformations in this region.²⁰ Thus, heteroaggregated SnO₂–TiO₂ nanoparticle networks represent an ideal model system to explore the potential of surface charge-induced heteroaggregation with regard to the generation of heterojunctions that enhance the separation of photogenerated charges.

EXPERIMENTAL SECTION

Synthesis. TiO₂ and SnO₂ nanoparticles were prepared by metal organic chemical vapor synthesis (MO-CVS) based on the decomposition of either titanium(IV) isopropoxide (Aldrich, 99.999% trace metals basis) or tetra-*n*-butyltin (Aldrich, technical grade, > 93%) vapor at $T = 1073$ K in a flow reactor system. The details of this technique are given elsewhere.²¹ For purification, the obtained powder samples were subjected to thermal treatment under high vacuum conditions. First, the powder sample was heated to $T = 870$ K using a rate of $r \leq 5$ K min^{−1}. Subsequent oxidation with O₂ at this temperature followed by cooling in O₂ atmosphere was successfully applied to remove organic remnants originating from the precursor material, on the one hand, and to guarantee the stoichiometric composition of the oxide on the other. The average particle size determined by transmission electron microscopy (TEM) and nitrogen sorption was 13 nm for TiO₂²⁷ and 10 nm for SnO₂ nanoparticles.

For the preparation of mixed ensembles of TiO₂ and SnO₂ nanoparticles, 250 mg of the powder samples were dispersed in 100 mL of $c = 10^{-6}$ mol·L^{−1} formic acid solution for 30 min under ultrasonication (Hielscher Sonifier 200S) and simultaneous agitation by a magnetic stirrer. Cooling with an ice–water mixture was applied to avoid unwanted sample heating. Centrifugation and subsequent drying in vacuum at room temperature resulted in the formation of monolithic pieces, which were transferred to a quartz glass cell and annealed to $T = 873$ K at $p < 10^{-5}$ mbar prior to spectroscopic

investigations. Prior to liquid exposure TiO_2 – SnO_2 nanoparticles were mixed in the desired 1:1 particle ratio.

Characterization. Zeta potentials and agglomerate size distributions of suspensions of 2.5 g oxide nanoparticles·L⁻¹ formic acid solution were derived from dynamic light scattering measurements on a Malvern ZetaSizer Nano ZS. Nitrogen sorption isotherms were obtained at $T = 77$ K using nitrogen adsorption/desorption (Quantachrome NOVA 4000e). Samples were degassed for 2 h in the degas unit of the adsorption apparatus at $T = 473$ K under vacuum prior to analysis. The BET surface area S_{BET} was evaluated using adsorption data in a relative pressure range p/p_0 from 0.05 to 0.2.²² The pore size distribution was calculated by applying the Barrett–Joyner–Halenda (BJH) model using the desorption branch of the isotherm.²³

Scanning electron microscopy (SEM) measurements were performed on a Zeiss Gemini Ultra 55 microscope operating at 20 kV equipped with an energy dispersive X-ray emission (EDX) detector. To characterize the mixing quality inside the nanoparticle networks we used EDX to track compositional homogeneity changes in the range of a few hundreds of nanometers. The local resolution of chemical information for EDX analysis is limited to the penetration depth and scattering of the primary electrons and therefore to the volume where characteristic X-rays are emitted of the sample. With acceleration voltages of 20 kV, the sampled volume in EDX studies is on the order of a few cubic micrometers for bulk TiO_2 or SnO_2 samples. Consequently, the determination of absolute Ti and Sn concentrations via EDX at the nanometer scale is not feasible. Nevertheless, by scanning the aggregate with a linescan, the change in the ratio between Ti and Sn can be tracked with a very high spatial resolution of approximately 100 nm.²⁴

For EPR measurements, the powder sample was contained within a Suprasil quartz glass tube connected to an appropriate high vacuum pumping system with a base pressure $p = 10^{-6}$ mbar. This allows for thermal sample activation and UV irradiation in situ. A 300 W Xe lamp (Oriol) was used as UV source. The light beam was passed through a water filter to exclude IR contributions from the excitation spectrum. Light power was measured with a bolometer (International Light). It was held constant at $P_{\text{irr}} = 0.9$ mW·cm⁻² for the energy range 3.2 eV < E < 6.2 eV throughout all experiments. During UV exposure, the samples were held at a temperature between $T = 90$ K and $T = 140$ K in order to keep UV-induced heating effects constant. X-band EPR measurements were performed on a Bruker EMX Micro spectrometer using a Bruker ER 4119 HS resonator. For measurements in the temperature range between $T = 90$ K and $T = 140$ K, an ER 4131 VT variable-temperature accessory was used. EPR computer simulations were done using the SIM 14S program.²⁵ The g values were determined on the basis of a DPPH standard.

RESULTS AND DISCUSSION

The procedure of particle aggregation as outlined by Figure 1 aims at the conversion of aerosol metal oxide nanoparticle powders, of high purity and well characterized particle surface properties,^{26,27} into binary metal oxide nanoparticle networks of high mixing quality and therefore with high concentrations of solid–solid heterointerfaces (Figure 1b).^{28,18} Prior to the process, aggregation between particles must be avoided in the starting mixture in order to achieve nanoparticle networks of different and perfectly intermixed metal oxides. Dynamic light

scattering experiments on dispersions of vapor phase-grown TiO_2 nanoparticles with an average particle size of 13 nm as determined by TEM²⁷ clearly demonstrate that metal oxide nanoparticles that were grown by MO-CVS can be efficiently deagglomerated by ultrasonic treatment in aqueous dispersion (Figure 3). As a consequence of ultrasonification, the

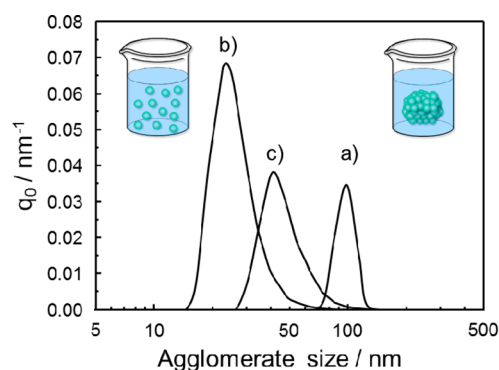


Figure 3. Size distribution profiles determined by dynamic light scattering experiments on dispersions of vapor phase-grown TiO_2 nanoparticles with an average particle size of 13 nm in $c = 10^{-6}$ mol·L⁻¹ formic acid. Ultrasonic treatment breaks up particle agglomerates and leads to the shift of the agglomerate size distribution maximum from (a) 100 nm to (b) approximately 20 nm. After 15 min of reagglomeration, which occurs after discontinuation of ultrasonic treatment, the maximum increases to approximately 40 nm (c).

agglomerate size distribution maximum shifts from 100 nm (Figure 3a) to 20 nm (Figure 3b). After discontinuation of ultrasonic treatment, particles reaggregate, and the agglomerate size distribution maximum shifts to approximately 40 nm (Figure 3c).

Zeta potential measurements reveal that both oxides carry a negative surface charge in neutral aqueous dispersion (Figure 4). As a result of particle aggregation, TiO_2 and SnO_2 form a nonuniform network which has a significant fraction of TiO_2 – TiO_2 and SnO_2 – SnO_2 interfaces. Self-assembly of oppositely charged particles in colloidal dispersion and, in consequence, the generation of desired TiO_2 – SnO_2 heterointerfaces is achievable via control of the surface

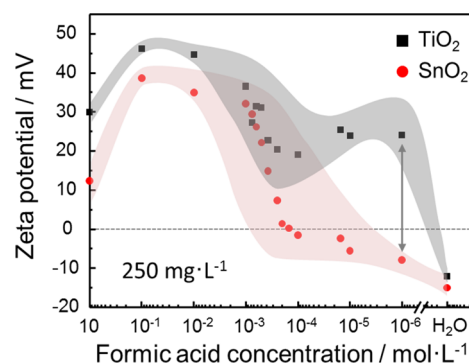


Figure 4. Zeta potentials of TiO_2 and SnO_2 nanoparticle samples in aqueous dispersion as a function of formic acid concentration. The shaded areas indicate the uncertainty of measurement. Prior to zeta potential measurements, all metal oxide samples were subjected to vacuum annealing and subsequent oxidation treatment at elevated temperatures to eliminate unintended effects that could originate from surface impurities.

charge.^{29–31} In comparison to inorganic acids, which potentially contaminate the particle surface with ions such as Cl^- , carboxylic acids are eligible candidates for surface charge adjustment since they can be efficiently eliminated from the particle network via oxidation at elevated temperatures. The zeta potential dependence of TiO_2 and SnO_2 nanoparticles on the formic acid concentration (Figure 4) prompted us to choose a formic acid concentration of $c = 10^{-6} \text{ mol}\cdot\text{L}^{-1}$ (indicated by gray arrow) where the zeta potential of TiO_2 and SnO_2 particles is +24 mV and –9 mV, respectively.

Surface charge adjustment for dispersed particles in combination with control over the pH in solution shows a complex functional dependence on the formic acid concentration. This is due to the formate adsorption equilibria at the metal oxide particle surfaces which, in turn, are subject to particle concentration in the dispersion and on the concentration of the acid and, concomitantly, on the pH.^{32,33} (For further details please see Supporting Information, Figure S1.)

Dehydration and dehydroxylation as well as oxygen treatment of the obtained particle networks at elevated temperatures were applied in order to eliminate organic surface groups that previously lead to surface charging and heteroaggregation.^{34,29} X-ray diffraction, TEM, and N_2 sorption measurements were carried out to identify potential process-induced structural changes that may result from hydration- and annealing procedures. All methods unambiguously reveal that primary particle properties size, structure, and morphology have been retained (Supporting Information, Figure S2).

Changes in the adsorption desorption hysteresis of nitrogen sorption experiments (left panel of Figure 5) clearly

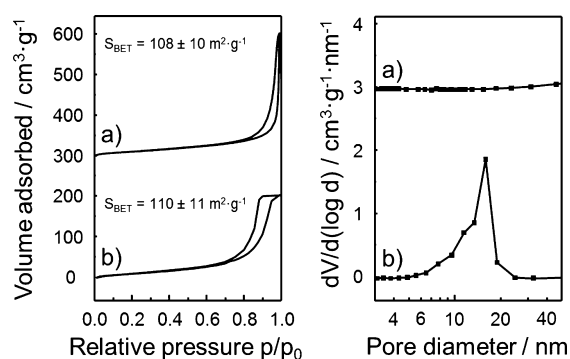


Figure 5. Sorption isotherms (left) and BJH pore size distributions (right) of SnO_2 – TiO_2 nanoparticle ensembles before (a) and after formation of heterointerfaces (b) in aqueous formic acid dispersion. The sorption isotherms and pore size distributions are shifted on the ordinate scale for $300 \text{ cm}^3\cdot\text{g}^{-1}$ and $3 \text{ cm}^3\cdot\text{g}^{-1}\cdot\text{nm}^{-1}$, respectively, for clarity.

demonstrate that loose nanoparticles transform into a mesoporous network,¹⁷ which are made up from interconnected particles and show a distinct pore size distribution (right panel of Figure 5b).

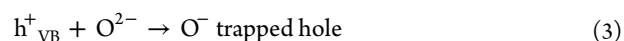
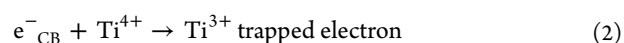
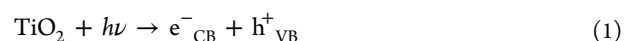
We employed SEM to characterize the composition and mixing quality inside the nanoparticle networks and used EDX to track compositional homogeneity changes in the range of few hundreds of nanometers.²⁴ A typical EDX line scan on nanoparticle networks obtained from surface charge-induced heteroaggregation in aqueous formic acid solution ($c = 10^{-6} \text{ mol}\cdot\text{L}^{-1}$) is shown in Figure 6a and reveals that the ratio of the two elements should remain constant across the scanned distance (gray line). The mixing quality and thus the

concentration of SnO_2 – TiO_2 heterojunctions is expected to be significantly higher than in the water processed networks. Here, deviations of the desired Ti to Sn ratio point to a nonuniform distribution of the two elements (gray line in Figure 6b) and therefore to the low mixing quality of the network.

The here presented procedure provides a very good measure of the local mixing quality within the nanoparticle networks. To obtain statistical meaningful information throughout different nanoparticle network samples, we evaluated the deviation of the desired ratio of Ti/Sn for approximately 600 sample spots (Figure 7). Deviations of 0% indicate that the chosen value of one TiO_2 particle per SnO_2 particle has been achieved. It can be shown that the nanoparticle network that originates from processing in pure water displays a very broad distribution of Ti/Sn deviation, while the network which was prepared in aqueous formic acid exhibits excellent mixing quality, i.e., relatively small deviations from desired Ti/Sn ratio.

A good mixing quality of SnO_2 and TiO_2 nanoparticle mixtures represents a necessary requirement for a high concentration of heterojunctions inside the resulting particle network. To verify that these solid–solid interfaces are truly suitable for interfacial charge transfer, we spectroscopically probed the photoelectronic materials' properties. For this purpose we utilized EPR to track the photogeneration of surface trapped hole centers O^- , unpaired electrons in shallow trap states Ti^{3+} or adsorbed O_2^- ions (Supporting Information).²⁷ As demonstrated by previous studies this technique provides site specific information about charge trapping sites.^{3,35–38} Band gap and conduction band edge energies determine the pathway of electrons or holes from one oxide to the other (Figure 2). The relative positions of the conduction band minima favor electron transfer from TiO_2 to SnO_2 . On the other hand, the valence band positions of the two oxides are such that photogenerated hole centers become accumulated on TiO_2 nanoparticles.

In Figure 8a, a simulated EPR spectrum of O^- and Ti^{3+} centers is shown in comparison to an experimental spectrum (b), which was acquired on dehydroxylated TiO_2 nanoparticles after 30 min of UV/Vis exposure under high vacuum conditions. The separation of photoexcited states (eq 1) is followed by persistent trapping of electrons and holes upon formation of Ti^{3+} and O^- centers, respectively (eqs 2 and 3).



The corresponding EPR spectrum of SnO_2 nanoparticles shows no significant signals after irradiation and is therefore not presented here.

After irradiation of a nanoparticle network of low mixing quality, the corresponding EPR spectrum reveals the presence of O^- and Ti^{3+} stabilized on TiO_2 nanoparticles (Figure 8c). However, the network prepared from surface charge induced heteroaggregation in aqueous formic acid solution shows a strong signal for O^- stabilized on TiO_2 nanoparticles but no Ti^{3+} centers (Figure 8d). Their absence points to an efficient interfacial electron transfer from TiO_2 particles to SnO_2 particles (Figure 2) upon formation of EPR silent states. For corroboration of this assumption, we exposed the samples after UV exposure to molecular oxygen ($p = 10 \text{ mbar}$). In the case of

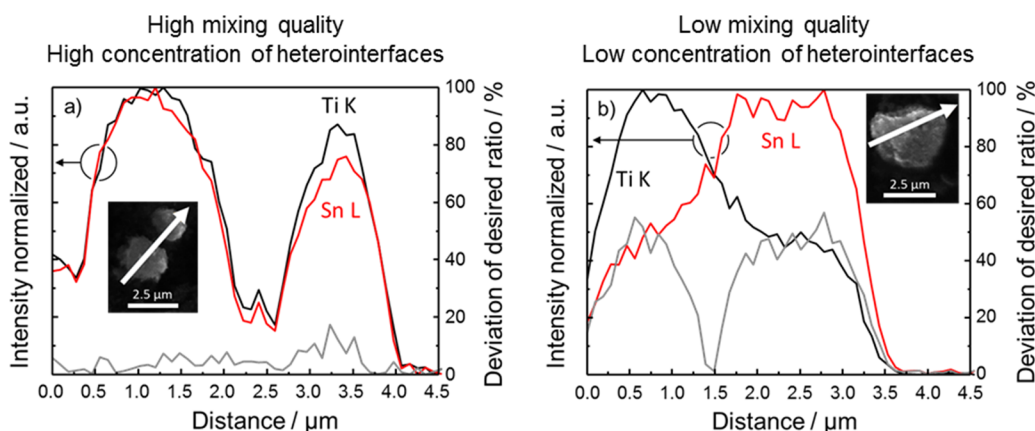


Figure 6. Characteristic EDX linescans of TiO_2 – SnO_2 networks obtained by heteroaggregation in (a) aqueous formic acid solution ($c = 10^{-6} \text{ mol}\cdot\text{L}^{-1}$) and (b) water. Scanned paths are shown in the SEM insets. The black and red lines show the distribution of Ti and Sn within the scanned distance. The gray line indicates the deviation of the desired Ti/Sn ratio.

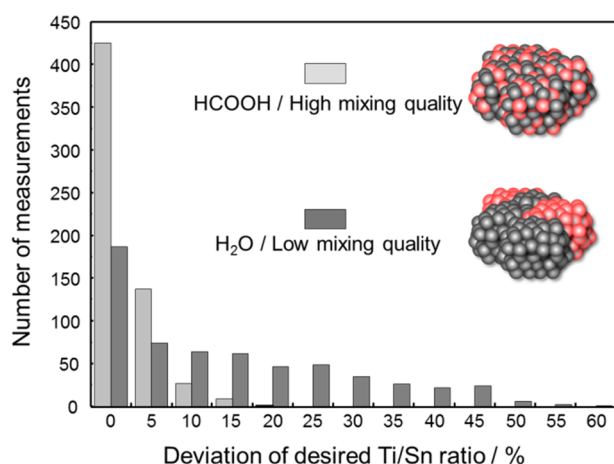
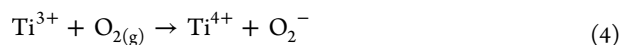


Figure 7. Statistical analysis of the mixing quality throughout the powder samples. Deviations of the desired Ti/Sn ratios within line scans of several micrometers across the particle networks are plotted in the diagram. The samples were prepared in $c = 10^{-6} \text{ mol}\cdot\text{L}^{-1}$ aqueous formic acid solution (HCOOH/High mixing quality) and water (H_2O /Low mixing quality).

TiO_2 nanoparticles, photogenerated electrons transfer to O_2 and form paramagnetic superoxide anions (O_2^-) (eqs 4 and 5), which remain stabilized on the particle surface and give rise to characteristic EPR signal signatures (Table 1, Figure 9a).²⁷



The redox potential of O_2/O_2^- (Figure 2 gray dotted line, $E = -4.22 \text{ eV}^{35}$) is slightly above the conduction band minimum of SnO_2 ($E_{\text{CB}} = -4.5 \text{ eV}^{39}$), which inhibits the transfer of SnO_2 related conduction band electrons to molecular oxygen and, thus, the formation of surface adsorbed O_2^- ions.⁴⁰ Figure 9 shows EPR spectra of the preirradiated metal oxide samples after 15 min oxygen exposure at $T = 90 \text{ K}$ and subsequent pumping to $p < 10^{-6} \text{ mbar}$. In the case of TiO_2 nanoparticles (a), a superimposition of O^- and O_2^- signal components is observed. The EPR parameters are given in Table 1.

Additional EPR resonances are observed on the network of low mixing quality (b) and attributed to O_2^- radicals, which are stabilized on SnO_2 surfaces (Table 1).^{40,41} For the network of

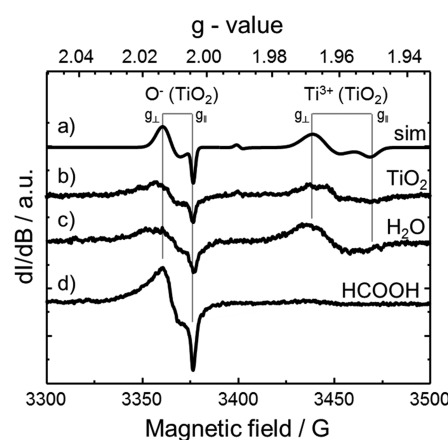


Figure 8. EPR spectra of metal oxide samples after 30 min UV/Vis light exposure ($P_{\text{irr}} = 0.9 \text{ mW}\cdot\text{cm}^{-2}$ for the energy range $3.2 \text{ eV} < E < 6.2 \text{ eV}$). (a) Simulated EPR spectrum of O^- and Ti^{3+} centers on TiO_2 nanoparticles. (b) Experimental EPR spectrum of O^- and Ti^{3+} centers on TiO_2 nanoparticles. (c) EPR spectrum of the sample with low mixing quality. (d) EPR spectrum of the sample with high mixing quality. All spectra were acquired at $T = 90 \text{ K}$ and $p < 10^{-6} \text{ mbar}$ using a microwave power of $P_{\text{MW}} = 6.32 \text{ mW}$.

Table 1. EPR Parameters of Radicals Observed on TiO_2 and SnO_2 Nanoparticle Surfaces as a Result of Charge Trapping

	Ti^{3+} [I]	Ti^{3+} [II]	O^- (TiO_2)	O_2^- (TiO_2)	O_2^- (SnO_2)
g_1	1.9660	1.9904	2.0126	2.0183	2.0235
g_2	1.9510	1.9600	2.0045	2.0094	2.0088
g_3				2.0033	2.0029

high mixing quality, no O_2^- stabilized on TiO_2 are observed in the EPR spectrum (c). From the absence of O_2^- ions we infer that all photogenerated electrons are drained into SnO_2 (Figure 2). This is different from TiO_2 , where photogenerated electrons, irrespective of whether they localize in shallow trap states (Ti^{3+}) or whether they remain in the conduction band,⁴² readily transfer to molecular oxygen.

For particle systems that were only in contact with pure water and dehydrated thereafter, there are no corresponding interfacial charge transfer effects. Obviously, related networks contain too many regions where TiO_2 or SnO_2 particles are aggregated in such a way that interfaces between identical metal

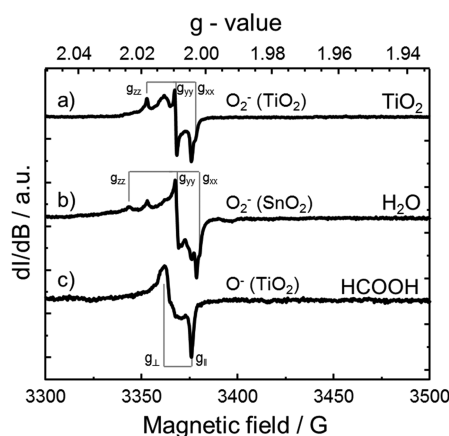


Figure 9. EPR spectra of preirradiated metal oxide samples after oxygen exposure ($p(\text{O}_2) = 10$ mbar). (a) EPR spectrum of O^- and O_2^- species stabilized on MO-CVS TiO_2 nanoparticles. (b) EPR spectrum of the sample with low mixing quality. (c) EPR spectrum of the sample with high mixing quality. The spectra were acquired at $T = 90$ K and $p < 10^{-6}$ mbar using a microwave power of $P_{\text{MW}} = 0.2$ mW. For better comparison, they were normalized and therefore do not carry any quantitative information.

oxide particles types prevail. Corresponding solid–solid interfaces were found to actually enhance the recombination of photogenerated charge carriers.²⁸ The quantitative analysis of persistently trapped photogenerated charges on the three different powder samples shows no concentration increase of stabilized hole centers (O^- radicals) for the water prepared network with low mixing quality in comparison to the pure MO-CVS TiO_2 nanoparticles (Figure 10). However, a strong enhancement of the concentration of O^- radicals was observed for the sample of high mixing quality.

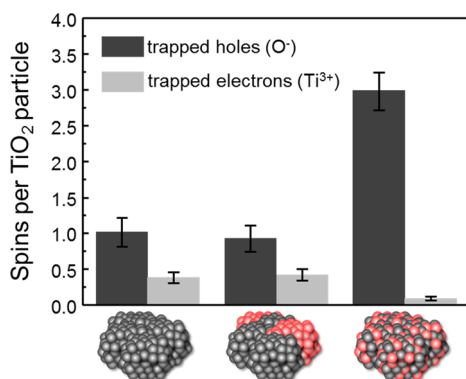


Figure 10. Quantitative assessment of trapped photogenerated charges on TiO_2 nanoparticles. The metal oxide samples were irradiated for 15 min ($P_{\text{irr}} = 0.9 \text{ mW} \cdot \text{cm}^{-2}$ for the energy range $3.2 \text{ eV} < E < 6.2 \text{ eV}$) at $T = 90$ K and $p < 10^{-6}$ mbar.

The quantitative analysis of the yield of photogenerated charges clearly shows that the adjustment of surface charge during particle network formation allows for the achievement of high mixing qualities and enables the realization of a high concentration of heterojunctions that are vital for the separation of photogenerated electrons and holes. The here presented results clearly underline the necessity to characterize and annihilate charge recombination on photoactive materials.

Surface charge-directed aggregation of different types of particles and the subsequent introduction of functional

interfaces is a cheap and versatile particle engineering approach to generate high concentrations of heterojunctions inside particle-based devices for photochemical application and energy production.

CONCLUSIONS

We intentionally introduced functional particle interfaces between two types of metal oxide nanoparticles and quantitatively determined the yield of photogenerated and trapped charges.²⁸ To yield blended nanoparticle systems hosting high concentrations of heterointerfaces, it is vital to prepare nanoparticles that subsequently can be easily deagglomerated in colloidal dispersion and to control the process of interface formation via surface charge induced heteroaggregation. As shown in this study, MO-CVS-grown particles can be simply dispersed by use of ultrasonic treatment to the single particle level. Controlled interface formation was achieved via heteroaggregation, i.e., via the self-assembly of oppositely charged particles in colloidal dispersion using formic acid for the adjustment of surface charge. In comparison to mixed particle systems prepared in pure water via surface charge-directed aggregation-prepared mixed particle systems show a substantially increased yield for photogenerated hole centers. The extremely high concentration of SnO_2 – TiO_2 heterojunctions actually gives rise to an enhanced cross section for the separation of photogenerated charges, which results from an effective interfacial charge transfer across the particle–particle interfaces.

ASSOCIATED CONTENT

Supporting Information

Further information concerning the crystallographic structure, the adsorption of formic acid, and the quantitative EPR measurements. This material is available free of charge via the Internet at <http://pubs.acs.org>.

AUTHOR INFORMATION

Corresponding Author

*E-mail: o.diwald@lfg.uni-erlangen.de.

Notes

The authors declare no competing financial interest.

ACKNOWLEDGMENTS

The authors thank Deutsche Forschungsgemeinschaft (DFG) for funding this project within the Research Training Group 1161 “Disperse Systems for Electronic Applications”. S.B. and O.D. acknowledge support from the Austrian Fonds zur Förderung der Wissenschaftlichen Forschung FWF-PI312 (ERA Chemistry). This work also made use of the facilities of the Cluster of Excellence “Engineering of Advanced Materials” at the University of Erlangen–Nuremberg.

REFERENCES

- (1) Zhang, H.; Chen, G.; Bahnemann, D. W. *J. Mater. Chem.* **2009**, 19 (29), 5089.
- (2) Kudo, A.; Miseki, Y. *Chem. Soc. Rev.* **2008**, 38 (1), 253.
- (3) Henderson, M. A. *Surf. Sci. Rep.* **2011**, 66 (6–7), 185–297.
- (4) Fujishima, A.; Zhang, X.; Tryk, D. A. *Sur. Sci. Rep.* **2008**, 63 (12), 515–582.
- (5) Maeda, K.; Domen, K. *J. Phys. Chem. Lett.* **2010**, 1 (18), 2655–2661.
- (6) Kamat, P. V. *J. Phys. Chem. Lett.* **2012**, 3 (5), 663–672.
- (7) Kamat, P. J. *Phys. Chem. C* **2007**, 111 (7), 2834–2860.

- (8) Kamat, P. V. *J. Phys. Chem. C* **2008**, *112* (48), 18737–18753.
- (9) Ritterskamp, P.; Kuklya, A.; Wüstkamp, M.-A.; Kerpen, K.; Weidenthaler, C.; Demuth, M. *Angew. Chem., Int. Ed.* **2007**, *46* (41), 7770–7774.
- (10) Kamat, P. V.; Tvrđy, K.; Baker, D. R.; Radich, J. G. *Chem. Rev.* **2010**, *110* (11), 6664–6688.
- (11) Wei, W.; Jha, H.; Yang, G.; Hahn, R.; Paramasivam, I.; Berger, S.; Spiecker, E.; Schmuki, P. *Adv. Mater.* **2010**, *22* (42), 4770–4774.
- (12) Tricoli, A.; Pratsinis, S. E. *Nat. Nanotechnol.* **2009**, *5* (1), 54–60.
- (13) Litschauer, M.; Neouze, M.-A. *J. Mater. Chem.* **2008**, *18* (6), 640.
- (14) Cardiel, A. C.; Benson, M. C.; Bishop, L. M.; Louis, K. M.; Yeager, J. C.; Tan, Y.; Hamers, R. J. *ACS Nano* **2012**, *6* (1), 310–318.
- (15) Buonsanti, R.; Grillo, V.; Carlino, E.; Giannini, C.; Gozzo, F.; Garcia-Hernandez, M.; Garcia, M. A.; Cingolani, R.; Cozzoli, P. D. *J. Am. Chem. Soc.* **2010**, *132* (7), 2437–2464.
- (16) Carbone, L.; Cozzoli, P. D. *Nano Today* **2010**, *5* (5), 449–493.
- (17) Elser, M. J.; Berger, T.; Brandhuber, D.; Bernardi, J.; Diwald, O.; Knözinger, E. *J. Phys. Chem. B* **2006**, *110* (15), 7605–7608.
- (18) Baumann, S. O.; Elser, M. J.; Auer, M.; Bernardi, J.; Hüsing, N.; Diwald, O. *Langmuir* **2011**, *27* (5), 1946–1953.
- (19) Bedja, I.; Kamat, P. V. *J. Phys. Chem.* **1995**, *99* (22), 9182–9188.
- (20) Pan, J.; Hühne, S.-M.; Shen, H.; Xiao, L.; Born, P.; Mader, W.; Mathur, S. J. *J. Phys. Chem. C* **2011**, *115* (35), 17265–17269.
- (21) Benfer, S.; Knözinger, E. *J. Mater. Chem.* **1999**, *9* (5), 1203–1209.
- (22) Brunauer, S.; Emmett, P. H.; Teller, E. *J. Am. Chem. Soc.* **1938**, *60* (2), 309–319.
- (23) Barrett, E. P.; Joyner, L. G.; Halenda, P. P. *J. Am. Chem. Soc.* **1951**, *73* (1), 373–380.
- (24) X-Ray diffraction as well as quantitative analysis like ICP-OES (inductively coupled plasma optical emission spectrometry) provide an integral value of the composition of the sample but do not carry any information about local distribution of elements within a defined volume. The local resolution of chemical information for EDX analysis is limited to the penetration depth and scattering of the primary electrons and therefore to the volume where characteristic X-rays are emitted of the sample. With acceleration voltages of 20 kV, the sampled volume in EDX studies are on the order of a few cubic micrometers for bulk TiO₂ or SnO₂ samples. Consequently the determination of absolute Ti and Sn concentrations via EDX at the nanometer scale is not feasible. Nevertheless, by scanning the aggregate with a linescan, the change in the ratio between Ti and Sn can be tracked with a very high spatial resolution of approximately 100 nm. In the case of binary mixtures with a high mixing quality, the ratio of two different elements should stay constant across the scanned distance (Figure 6a, gray line). Deviations of the desired Ti to Sn ratio point to a nonuniform distribution of the two elements and therefore to low mixture quality of the network (Figure 6b, gray line).
- (25) Lozos, G. P. *SIM14S*, EPR spectrum simulation, 1996.
- (26) Siedl, N.; Elser, M. J.; Halwax, E.; Bernardi, J.; Diwald, O. *J. Phys. Chem. C* **2009**, *113* (21), 9175–9181.
- (27) Berger, T.; Sterrer, M.; Diwald, O.; Knözinger, E. *ChemPhysChem* **2005**, *6* (10), 2104–2112.
- (28) Siedl, N.; Elser, M. J.; Bernardi, J.; Diwald, O. *J. Phys. Chem. C* **2009**, *113* (36), 15792–15795.
- (29) López-López, J. M.; Schmitt, A.; Moncho-Jordá, A.; Hidalgo-Álvarez, R. *Soft Matter* **2006**, *2* (12), 1025.
- (30) Piechowiak, M. A.; Videcoq, A.; Ferrando, R.; Boichichio, D.; Pagnoux, C.; Rossignol, F. *J. Phys. Chem. Chem. Phys.* **2012**, *14* (4), 1431.
- (31) Piechowiak, M. A.; Videcoq, A.; Rossignol, F.; Pagnoux, C.; Carrion, C.; Cerbelaud, M.; Ferrando, R. *Langmuir* **2010**, *26* (15), 12540–12547.
- (32) Mpandou, A.; Siffert, B. *J. Colloid Interface Sci.* **1984**, *102* (1), 138–145.
- (33) Zhao, J.; Hidaka, H.; Takamura, A.; Pelizzetti, E.; Serpone, N. *Langmuir* **1993**, *9* (7), 1646–1650.
- (34) Cerbelaud, M.; Videcoq, A.; Abélard, P.; Pagnoux, C.; Rossignol, F.; Ferrando, R. *Soft Matter* **2010**, *6* (2), 370–382.
- (35) Fujishima, A.; Rao, T. N.; Tryk, D. A. *J. Photochem. Photobiol., C* **2000**, *1* (1), 1–21.
- (36) D'Arienzo, M.; Carbajo, J.; Bahamonde, A.; Crippa, M.; Polizzi, S.; Scotti, R.; Wahba, L.; Morazzoni, F. *J. Am. Chem. Soc.* **2011**, *133* (44), 17652–17661.
- (37) Macdonald, I. R.; Howe, R. F.; Zhang, X.; Zhou, W. *J. Photochem. Photobiol., A* **2010**, *216* (2–3), 238–243.
- (38) Dimitrijevic, N. M.; Rozhkova, E.; Rajh, T. *J. Am. Chem. Soc.* **2009**, *131* (8), 2893–2899.
- (39) Yong, X.; Schoonen, M. A. A. *Am. Mineral.* **2000**, *85* (3–4), 543–556.
- (40) In fact, we evidence O^{•−} signals that results from UV exposure as well as an O₂^{•−} signal after oxygen exposure of MO CVS SnO₂ nanoparticles. Both types of signals are by a factor of ~100 lower in intensity and therefore negligible with respect to signals of the other samples discussed in this study.
- (41) Meriaudeau, P.; Naccache, C.; Tench, A. J. *J. Catal.* **1971**, *21* (2), 208–211.
- (42) Berger, T.; Sterrer, M.; Diwald, O.; Knözinger, E.; Panayotov, D.; Thompson, T. L.; Yates, J. T., Jr. *J. Phys. Chem. B* **2005**, *109* (13), 6061–6068.